IEEE Access
Multidisciplinary | Rapid Review | Open Access Journal

Received January 29, 2021, accepted February 15, 2021, date of publication February 22, 2021, date of current version March 8, 2021.

Digital Object Identifier 10.1109/ACCESS.2021.3061098

Optimal Tuning of the Current Loop for Dual-Loop Controlled Grid-Forming Converters Based on Active Damping Optimization

ZHIHONG ZHAO[1], ZHIPENG HAN[1], XUNDUAN LIU[1], JIA YAO[1], (Member, IEEE), BAOJIAN JI[1], SHUZHENG WANG[2], AND JIANFENG ZHAO[3]

[1]Department of Electrical Engineering, School of Automation, Nanjing University of Science and Technology, Nanjing 210096, China
[2]Jiangsu Collaborative Innovation Center for Smart Distribution Network, Nanjing 211167, China
[3]School of Electrical Engineering, Southeast University, Nanjing 210096, China

Corresponding author: Zhihong Zhao (zhaozhihongnjust@163.com)

This work was supported in part by the National Natural Science Foundation of China under Grant 51807092, and in part by the Open Research Fund of Jiangsu Collaborative Innovation Center for Smart Distribution Network, Nanjing Institute of Technology, under Grant XTCX202004.

ABSTRACT Effective sinusoidal voltage regulation is of permanent importance for grid-forming converters. Usually, the following two types of schemes are employed to achieve a high level of performance: 1) single-loop voltage and 2) dual-loop voltage-current control. The performance of both schemes has comprehensively been evaluated in this work, based on the developed discrete-time model of the LC-filtered grid-forming converter. The challenges of insufficient stability margin, constraint bandwidth, and high sensitivity to parameter variation faced by the single-loop control scheme have been addressed, if the high-performance resonant controllers are employed for voltage regulation. Alternatively, the dual-loop control does not experience such issues with the inclusion of inner-current loop which provides active damping for the overall system. The essence of the inner-current loop is identified based on the discrete root locus analysis. Also, to obtain the highest damping and most enhanced stability, the criterion for current loop design has been addressed and a method for optimal tuning of the inner-current loop is developed, where the original plant with the one-sampling delay and the current gain are considered as the equivalent plant for the voltage controller. Experimental results have verified the effectiveness of the developed method for regulation of grid-forming converters.

INDEX TERMS Active damping, LC filter, resonance, voltage regulation, current loop.

I. INTRODUCTION

Effective sinusoidal voltage regulation is an aspect of paramount importance for grid-forming converters (GFCs) to achieve a high level of performance in a lot of different applications, such as virtual synchronous machine (VSG)/droop control for grid-tied converters [1], [2], dynamic voltage restorers [3], [4], ground power units for airplanes [5], [6], uninterruptable power supplies [7]–[10], and auxiliary inverters for rail trains [11], [12], just to name a few. In particular, for applications where GFCs with VSG/droop control, or various enhanced methods [13], the converter also provides grid supporting for the grid or microgrid. Therefore, in these scenarios, GFCs presents as a voltage source to the load and/or grid, which means a stable ac output voltage with high waveform quality is generally required [5], [11]. In order to reduce the high frequency switching ripples, LC filters are commonly added to their output ac terminals [1], [12]–[25]. However, LC filters can cause stability problems related to resonance, which theoretically, can be passively damped by adding resisters in series or parallel with the capacitors, just like the case of LCL filters which have been the subject of significant researchers [26]–[30] in recent years. This way of damping is however inefficient, and the filter effectiveness can even be deteriorated. Therefore, active damping methods have been prefered, where the basic idea is to improve damping through modifying the control strategy, in place of the damping resisters [11]–[15], [26]. In this manner, additional

The associate editor coordinating the review of this manuscript and approving it for publication was Yijie Wang.

power loss can be avoided, and more importantly, filter effectiveness can still be retained.

Usually, either single-loop voltage or dual-loop voltage-current control can be employed for active damping of GFCs, depending on whether additional filter variables, which can either be its inductor- or capacitor-current, are sensed and fed back for regulation [5], [11], [12], [15], [31]–[34]. Regarding the single-loop control method, only the capacitor voltage is measured and fed back for regulation. This method avoids the high-resolution current sensors, which is therefore cost effective and easy to implement, and has, in fact, been used with same applications like in [5], [10] and [33]. It has been proved in these studies that the single-loop control has been suffered from the issue of poor stability, if resonant controllers are employed for voltage regulation. This is because the proportional gain has little help with improving the system's overall performance, but will reduce the stability margin instead. As a result, only resonant term is suggested [5], [33]. The stabilizing mechanism underlying this method is further investigated in [14], where it has been shown that the delays related to digital computation and modulation lead to a critical frequency for the LC-filter resonance, above which the system can be stabilized without any additional resonance damping. A negated low-pass filter added to the feedback path has also been suggested, which can be used to increase the stability region equivalently. Despite that, single-loop voltage control may still not an good choice for GFCs, which this paper will prove with a comprehensive evaluation about its performance, including the discrete root locus and Nyquist diagram analysis.

Dual-loop voltage-current control has therefore been preferred and implemented in [11], [15] and [31], where it has been shown that inner current loop can provide active damping for the overall control system. It therefore offers an effective way to resolve the issues faced by single-loop control scheme. In these studies, the one-sampling delay is approximated by either the first- or second-order Padé expression. However, this approximation may not appropriate for GFCs working with a low pulse ratio, i.e. the ratio of the switching frequency with respect to the frequency of the reference signal. This case happens in high-power converters that operating at a low-switching frequency, which is often required to reduce switching losses of semiconductor devices in high-power applications [35]. It is also the case for aeronautic applications, where fundamental frequency is between 400 and 800 Hz, like in [5] and [6]. It should be noted that even in cases in which fundamental frequency ω_e is not that high with respect to the switching frequency, controllers targeted for high frequency signal of $h\omega_e$ are usually included, in order to reject harmonics introduced by nonlinearities such as dead-time effect and/or nonlinear loads, resulting in improved disturbance rejection performance. With this under consideration, it is preferable to perform the study in the z-domain. As a consequence, it is necessary to establish the discrete model of LC-filtered GFCs, which has been addressed in several works like in [15] and [34]. In these studies, the capacitor voltage is treated as a disturbance and a feed forward approach is employed. This is a common practice for disturbance rejection in grid-following converters, which present a current source to the grid instead. In this manner, approximation is thus introduced, resulting in inaccurate or even unreliable results. To solve this issue, the accurate discrete-time model of LC-filtered GFCs is therefore developed in this paper. Performance evaluation of GFCs can then be performed in the z-domain directly, including stability analysis, current- and voltage-loop design.

On the other hand, regarding a dual-loop or multi-loop system, in order to fulfill the signal-regulation speed requirement between different loops, the bandwidth of the inner loop is commonly designed much higher than that of the outer loop [5], [11], [14], [15], [31], [32]. This rule is also followed by the literatures related to the dual-loop control of GFCs. For instance, the bandwidth of the outer-voltage loop is designed about to be one-tenth to one-fifth of that of the inner-current loop [11], [31]. In this manner, the current loop can be considered as an unity gain approximately within the bandwidth of the voltage loop, which is, therefore, convenient for the tuning of the voltage controller. This method is very popular, and has, in fact, been used in some applications like in [31] and [34]. However, the study in [5] claimed that for cases where GFCs working with a low pulse-ratio, it is not easy or even impossible to satisfy this requirement, as the one-sampling delay related to digital control can significantly deteriorate the performance and lead to a narrow bandwidth of the inner current loop. Other alternatives include setting the damping ratio of the current loop to 0.707 in [15] or unity in [18]. The modeling and analysis of these methods are however performed in the continues-time domain and the approximation is introduced not only for the Padé expression, but also for the inner-current loop transfer function, which will be proved in the following sections of this work.

On the other hand, with regard to the outer-voltage loop, resonant controllers (RCs) are commonly preferred for its excellent performance of tracking sinusoidal references of arbitrary frequencies with zero steady-state error for both positive- and negative-sequences. Commonly, the following two types of RCs are mainly employed to obtain high performance: 1) proportional resonant (PR) and 2) vector proportional integral (VPI). In particular, it has been proved that VPI is superior to PR for the plant that have the form of $1/(sL + R_L)$ in term of stability and overall parameter sensitivity. This is however not valid for the case of LC-filtered GFCs, because the frequency response of a L filter is quite different from that of a LC filter, as proved in this work. Also, in order to alleviate the adverse impacts of the delays introduced by the digital control and original plant, it is preferable to add a delay compensation technique to these controllers to improve stability. However, the majority of the literatures related to delay compensation have been dedicated to the current control of grid-following converters, and few works have addressed this issue concerning voltage regulation of GFCs. Despite that, the essence of the delay compensation

is the same for these two kinds of converters, i.e. to improve the system's stability and performance. Therefore, the techniques developed from gird-following converters can also be applied to GFCs. For instance, various predictive methods including the Smith predictor [36], the state observer [37], and the dead-beat control [38], have been developed. The effectiveness of these methods is highly dependent on the modeling accuracy built for the system. Other alternatives including the multisampling strategy [39] and those based on accurate derivatives [40], [41]. These methods mainly focus on the minimization of the impact of the one-sampling delay, leaving the delays related to the plant unconsidered. Particularly, based on the Nyquist diagrams and sensitivity function, the delay compensation of resonant controllers for current regulation of grid-following converters is addressed in [35]. This method is now extended to the voltage regulation of dual-loop controlled GFCs in this work, to obtain the desired stability and avoidance of closed-loop anomalous peaks.

It should be emphasized that design of the inner-current loop is the basis for that of the outer-voltage loop, which hence has a great impact on the system's stability and overall performance. It is therefore of much interest to investigate the principle to guide the tuning of the inner-current loop for dual-loop controlled GFCs, which is the main objective of this work. Specifically, for the inner-current loop design, the constraints faced by the loop-bandwidth method is identified, and a method based on active damping optimization is developed which addresses the original plant, the one-sample delay, and the current gain as the equivalent plant for the voltage controller, to obtain the highest damping and most enhanced stability. Also, the delay compensation for the voltage loop with PR controller employed is addressed. To do that systematically, Section II begins by establishing the model of LC-filtered GFCs in the z-domain. The single- and dual-loop control for GFCs are then compared more deeply in Section III, to better identify their features and constraints. This is followed by Section IV, where the creterion for the inner-current loop design is identified and a method for optimum tuning of the current loop to obtain the most enhanced stability is developed. The outer-voltage loop with PR controller employed is then analyzed step by step in Section V, where a delay compensation strategy is also presented. Effectiveness of the proposed design method is finally verified through experiments in Section VI, before concluding the findings in Section VII.

II. SYSTEM MODELING AND DESCRIPTION

Fig.1 shows a three-phase voltage-source GFCs with an output LC filter, where L is the filter inductor, and C is the filter capacitor. After the filter is an output transformer T, which is usually required for applications where isolation is essential. It should be noted that R_{L} is the series equivalent resistance, which is usually used for emulating the power losses of the converter (mainly from inductors and power switches). Also shown in this figure is the corresponding control structure with both single- and dual-loop control schemes included.

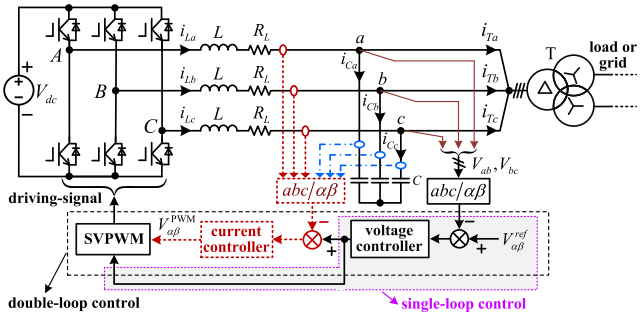

FIGURE 1. Three-phase GFCs with single- and dual-loop control schemes.

Specifically, if the current controller, whose feedback can either be the inductor current i_L or capacitor current i_C, is employed, the dual-loop control scheme results; otherwise, the single-loop control scheme with the capacitor voltage feedback is obtained.

To illustrate, the single- and dual-loop control schemes are further represented in Figs.2 and 3 respectively, where the continuous LC filter has been noted in the s-domain, and the digital controller has been noted in the z-domain. It should be noted that if R_{L} is ignored, i.e. $R_{\mathrm{L}} = 0$, then it emulates the worst case without any physical damping for the LC filter. From the inspection of Figs.2 and 3, the only difference noted between single- and dual-loop control schemes is the employment of current loop, which theoretically, provides active damping for the undamped LC filter. To better identify these differences, it is preferable to derive transfer functions in Figs.2 and 3 for representing the two different control methods respectively, beginning with the function in (1) for representing the plant

$$\left\{\left[V^{\mathrm{PWM}}(s) - V(s)\right]\frac{1}{sL} - I_T(s)\right\}\frac{1}{sC} = V(s). \qquad (1)$$

Transfer function for relating the controller output voltage V^{PWM} to the capacitor voltage V can therefore be derived as

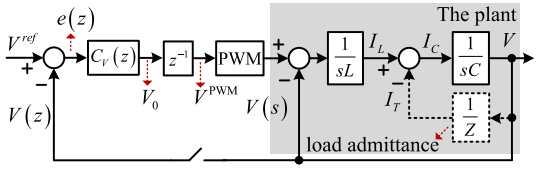

FIGURE 2. Single-loop voltage control scheme for GFCs.

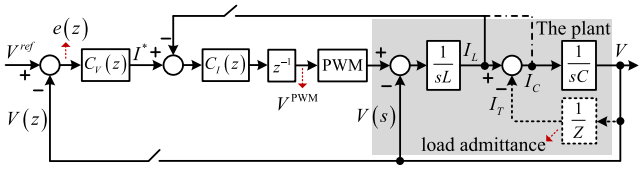

FIGURE 3. Dual-loop voltage-current control scheme for GFCs.

follows:

$$G_{\mathrm{V}}(s)=\frac{V(s)}{V^{\mathrm{PWM}}(s)}=\frac{1}{s^2LC+1}=\frac{\omega_{res}^2}{s^2+\omega_{res}^2} \tag{2}$$

where $\omega_{res}=\sqrt{1/L\cdot C}$ is the filter resonance frequency.

It should be noted that the load current I_{T} is treated as a disturbance and ignored both in Figs.2 and 3, which is reasonable since GFCs have to work in the no-load condition. This characteristic of GFCs, in fact, appears an antithetic relationship with that of grid-following converters, where grid voltage is considered as a disturbance instead. With regard to Figs.2 and 3, ideally, either single- or dual-loop control should have full rejection of this disturbance, which means the steady-state value of V excited form I_{T} will be zero. This is usually achieved through the employment of resonant controllers (RCs) for the voltage regulator $C_{\mathrm{V}}(z)$, whose open loop gain is infinite at the desired frequencies.

In this manner, as shown in Fig.3, feeding back I_{L} or I_{C} will produce the same result, which have comprehensively been studied in [15]. As a consequence, only the case of I_{L} feedback is considered in this paper, which can also be employed for the over current protection of the converter. For subsequent analysis, it is necessary to derive the transfer functions related to the inner-current loop, beginning with the expression of (3) shown below:

$$\begin{cases}\left[V^{\mathrm{PWM}}(s)-V(s)\right]\cdot\dfrac{1}{s\cdot L}=I_L(s)\\ \left[I_L(s)-I_T(s)\right]\cdot\dfrac{1}{s\cdot C}=V(s)\,.\end{cases} \tag{3}$$

Transfer function for relating the controller output voltage V^{PWM} to the inductor current I_{L} can, therefore, be derived as follows:

$$G_{iL}(s)=\frac{I_L(s)}{V^{\mathrm{PWM}}(s)}=\frac{s\cdot C}{s^2LC+1}=\frac{1}{L}\frac{s}{s^2+\omega_{res}^2}. \tag{4}$$

Expressions (2) and (4) can next be transformed to the z-domain by applying the zero-order holder discretization. The resulting transfer functions, noted in Fig.4 as $G_{\mathrm{V}}(z)$ and $G_{iL}(z)$, are given from (5) to (6) respectively, where T_s represents their common sampling period

$$G_{\mathrm{V}}(z)=\frac{(z+1)\cdot(1-\cos(\omega_{res}\cdot T_s))}{z^2-2z\cdot\cos(\omega_{res}\cdot T_s)+1} \tag{5}$$

$$G_{iL}(z)=\frac{1}{\omega_{res}\cdot L}\cdot\frac{\sin(\omega_{res}\cdot T_s)\cdot(z-1)}{z^2-2z\cdot\cos(\omega_{res}\cdot T_s)+1}. \tag{6}$$

On the other hand, with regard to RCs, transfer functions related to PR and VPI in the s-domain are given in (7) and (8), respectively, where the delay compensation φ is included

$$\begin{aligned}G_{\mathrm{PR}}^{d}(s)&=K_p+K_i\cdot\frac{s\cdot\cos\varphi-\omega_e\cdot\sin\varphi}{s^2+\omega_e^2}\\&=K_p+K_i\cdot R^{1d}(s)\end{aligned} \tag{7}$$

$$\begin{aligned}G_{\mathrm{VPI}}^{d}(s)&=K\cdot\frac{(sL+R_{\mathrm{L}})\left(s^2\cdot\cos\varphi-\omega_e\cdot\sin\varphi\right)}{s^2+\omega_e^2}\\&=K_p\cdot R^{2d}(s)+K_i\cdot R^{1d}(s)\,.\end{aligned} \tag{8}$$

In both expressions, ω_e is their common fundamental angular frequency, at which the final steady-state tracking error will be zero, while K_p and K_i are the proportional and resonant gains. For VPI controller, in particular, $K_p/K_i=L/R_{\mathrm{L}}$ is generally required to cancel coupling terms produced by the plant that can be modeled as $1/(sL+R_{\mathrm{L}})$. The RCs of (7) and (8) must also be discretized for digital implementation, whose transfer function after prewarped Tustin transformation are $G_{\mathrm{PR}}^{d}(z)=K_p+K_iR_{tp}^{1d}(z)$ and $G_{\mathrm{VPI}}^{d}(z)=K_pR_{tp}^{2d}(z)+K_iR_{tp}^{1d}(z)$, respectively. The expression of $R_{tp}^{1d}(z)$ and $R_{tp}^{2d}(z)$ can be appreciated from [35], which will not be elaborated here. Where necessary, additional resonant terms with ω_e replaced by $h\omega_e$ can also be included for the rejection of the h-order harmonic from the capacitor voltage, which can be introduced by the dead-time effect and/or nonlinear loads.

Expressions from (5) to (8) can eventually be merged to give the open-loop transfer functions for the analysis of single- and dual-loop control of GFCs, which will be discussed in the following sections.

III. ANALYSIS OF SINGLE-LOOP VOLTAGE CONTROLLED GFCs

As shown in Fig.4(a), if PR controller is employed for $C_{\mathrm{V}}(z)$, the open-loop transfer function for representing the single-loop control scheme can be derived as follows:

$$G_{\mathrm{OL}}^{V1}(z)=G_{\mathrm{PR}}^{d}(z)\cdot z^{-1}\cdot G_{\mathrm{V}}(z)\,. \tag{9}$$

The resonant term $R_{tp}^{1d}(z)$ is firstly ignored to evaluate the influence of K_p on the system's overall performance. Therefore, $G_{\mathrm{PR}}^{d}(z)=K_p$ results, which together with (5) substituted into (9), gives rise to

$$G_{\mathrm{OL}}^{V1}(z)=K_p\cdot\frac{(z+1)(1-\cos(\omega_{res}\cdot T_s))}{z\left(z^2-2z\cdot\cos(\omega_{res}\cdot T_s)+1\right)}. \tag{10}$$

Parameters of the LC filter are listed in Table 1. Then, by varying the proportional gain K_p, root locus depicted in Fig.5(a) representing (10) can be obtained. It can be noted

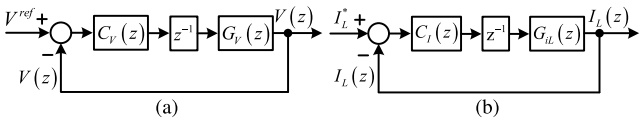

FIGURE 4. Structure of (a) single-voltage and (b) inner-current loop in the z-domain.

TABLE 1. Parameters of the LC filter.

Switch frequency	f_{sw}	3kHz
Sampling frequency	$f_s=2f_{sw}$	6kHz
Inductance	L	1mH
Capacitor	C	30μF
Series equivalent resistance	R_{L}	0.1Ω

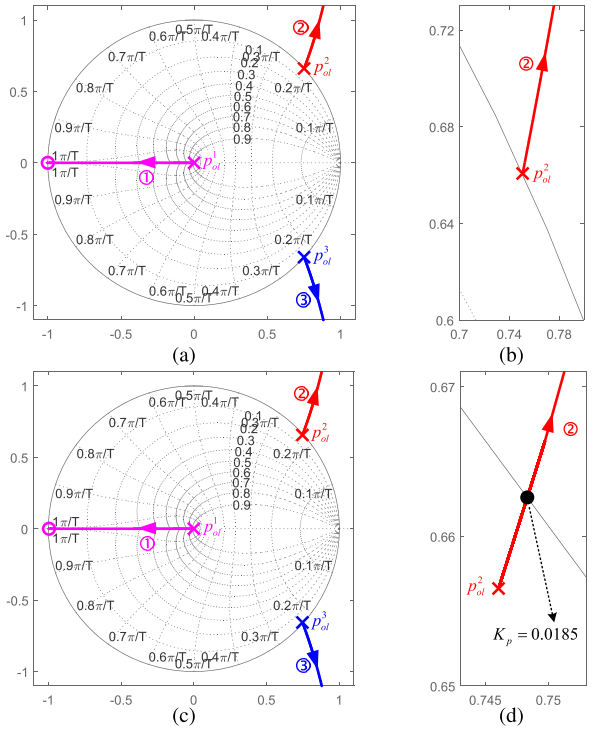

FIGURE 5. Root locus of (a) (9) with R_L ignored; (b) detailed part of (a) around p_{ol}^2; (c) (9) with R_L considered; (d) detailed part of (c) around p_{ol}^2.

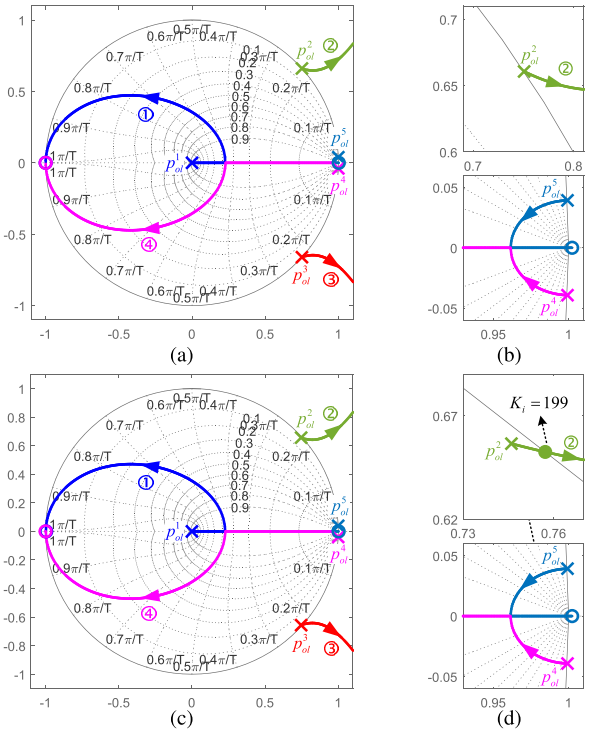

FIGURE 6. Root locus of (a) (9) with R_L ignored; (b) detailed part of (a) around p_{ol}^2 and p_{ol}^1; (c) (9) with R_L considered; (d) detailed part of (c) around p_{ol}^2 and p_{ol}^1.

that the pair of conjugate poles $p_{cl}^{2,3} = \cos(\omega_{res} \cdot T_s) \pm j \cdot |\sin(\omega_{res} \cdot T_s)|$, which are related to the filter resonance, are located exactly on the unit circle, as shown in Fig.5(b) for a clearer view. In particular, trajectories starting from $p_{cl}^{2,3}$ are always outside of the unit circle, which means the close-loop system is certainly unstable. Alternatively, if R_L is considered, $p_{cl}^{2,3}$ still reside very close to the unit circle, whose damping ratio is approximately 0.0087, as shown in Figs.5(c) and (d). Also, it can be noted from Fig.5(d) that $K_p < 0.0185$ is required to ensure stability. Unfortunately, the close-loop poles on cures ② and ③ will move toward to the unit circle with the increase of K_p, resulting in a reduced stability margin, which is certainly undesired.

Proportional gain K_p is therefore not generally recommended for the single-loop control of GFCs. In this manner, $G_{\mathrm{PR}}^d(z)$ can be simplified to $K_i R_{lp}^{1d}(z)$, which upon substituted into (9), root locus of Fig.6 plotted by varying the resonant gain K_i can be obtained. It can be noted that if R_L is ignored, trajectories starting from $p_{cl}^{2,3}$ are still located at the outside of the unit circle, as shown in Figs.6(a) and (b), just like the direct application of K_p in Fig.5(a). Similarly, in case R_L is included, K_i<199 is required to ensure a stable operation, which can be observed from Fig.6(d). However, the system stability is still poor even if this condition is satisfied, as the closed-loop poles on curves ② and ③ still lie very close to the unit circle. Similar analysis can also be performed for the case that VPI is employed for $C_V(z)$, where specifically, $K < 47$ is required to guarantee a stable operation.

The challenge faced by single-loop controlled GFCs is therefore its insufficient stability margin. This can further be identified from the inspection of the system's frequency response, as shown in Fig. 7 where VPI with $K = 25$ is employed for $C_V(z)$. It can be noted that the phase margin (PM) is 90.4 deg, as shown in Fig. 7(a). The system is therefore seems quite stable. This is however not true, as the system is very sensitive to the estimation error of R_L and L, which in practice, cannot be tracked precisely. For instance, if the estimated value of R_L deviates from its actual value by 30%, the minimum distance between the Nyquist trajectory and the critical point $(-1, 0j)$, i.e. η, is reduced to 0.18, as shown in Fig.7(b). The system stability is thus seriously deteriorated, even though PM remains the same. Therefore, single-loop controlled GFCs has a poor robustness against parameters detuning due to estimation errors in the value of the LC filter. On the other hand, the closed-loop bandwidth is only 1.31 Hz around the fundamental frequency, as shown in Fig. 7(c), resulting in a slow transient response of the output voltage, which is certainly unexpected.

IV. ANALYSIS AND DESIGN OF INNER-CURRENT LOOP FOR DUAL-LOOP CONTROLLED GFCs

Commonly, proportional K_C is employed for the current controller. With (5) and $C_I(z) = K_C$ now defined, the open-loop transfer function of Fig.4(b) for representing the inner-current loop can be derived. Performance evaluation of the inner-current loop can then be performed, which

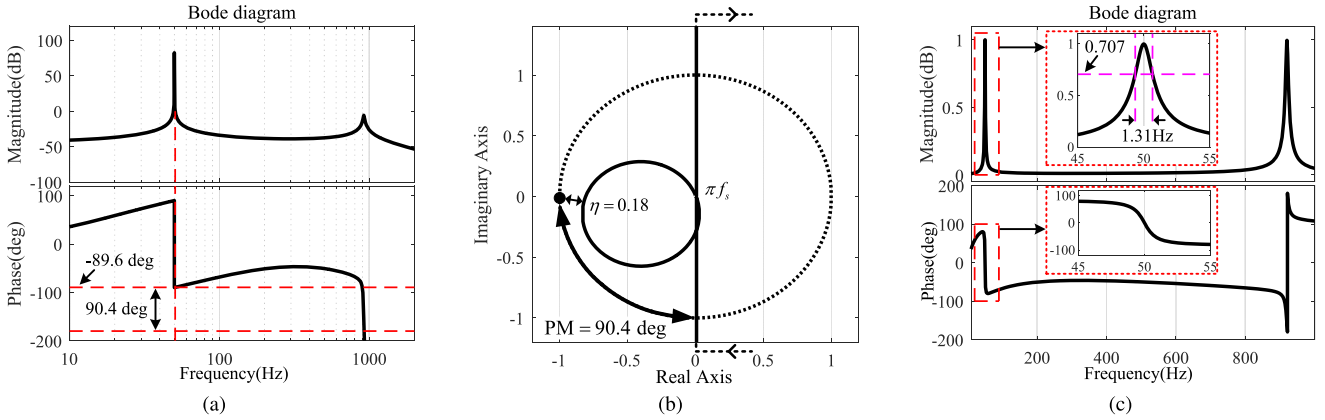

FIGURE 7. (a) open-loop frequency response, (b) Nyquist diagram and (c) closed-loop frequency response of single-loop voltage control scheme.

in [5], [12], [15], [31], and [32], the frequency response analysis is adopted. This method is however not suitable in this case, as it is hard or even impossible to determine the optimum gain for the current loop to get the most enhanced stability of GFCs. Because of that, a method based on damping optimization through the discrete root locus analysis is developed in this section, which addresses the original plant, the one-sample delay, and the current gain as the equivalent plant for the voltage controller, beginning with some analytical plots to better identify the constraints faced by existing methods.

A. FREQUENCY RESPONSE ANALYSIS OF THE INNER-CURRENT LOOP

To better identify the fundamental function of the inner-current loop, the method presented in [11], [12] and [31] is employed for comparison with the one developed in this work. The objective of this comparison can be summarized into two aspects: 1) to verify of the accuracy of the discrete model established previously and 2) to identify the intrinsic function of the current loop. Firstly, the transfer function related to the inner-current loop developed in [11] can be expressed as follows:

$$I_L = \frac{K_C \cdot e^{-sT_d}}{K_C \cdot e^{-sT_d} + sL} \left(I_L^* + \underbrace{V^{ref} e^{-sT_d} - V}_{\approx 0} \right) \qquad (11)$$

where $e^{-sT_d} \approx \left(1 - s\frac{1}{2}T_d\right) \Big/ \left(1 + s\frac{1}{2}T_d\right)$ is the delay block related to digital implementation and PWM modulation, which is approximated by the first-order Padé expression. It should be mentioned that T_d is the total delay of 1.5 times the sampling period, i.e. $T_d = 1.5T_s$.

It can be noted from (11) that $V = V^{ref} \approx V^{ref} e^{-sT_d}$, as long as high performance controllers are employed for $C_V(z)$ to achieve a non-steady-state tracking error of the output voltage V with respect to the reference signal V^{ref}. In this manner, the last term in the brace of (11) is approximated to zero and can be ignored. This approximation is however only true in the steady state, but not during transient. To better understand this inaccuracy in a direct way, some analytical plots are provided as follows.

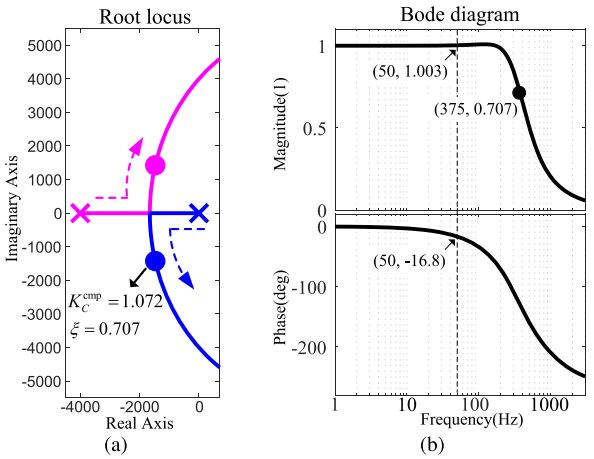

FIGURE 8. (a) the root locus of (11) which is plotted by varying the current gain K_C, (b) the closed-loop frequency response of (11) with $K_C^{cmp} = 1.072$ employed.

With the parameters in Table 1 defined, the root locus of (11) can be plotted, as shown in Fig.8(a), which is sketched by varying the current gain K_C. In particular, the study in [11] and [12] proposed that the gain resulting in $\xi = 0.707$ can be considered as the optimal choice, which in Fig.8(a), is noted as $K_C^{cmp} = 1.072$. Accordingly, the closed-loop frequency response is illustrated in Fig.8(b), where the bandwidth of 375 Hz can be appreciated, resulting in a good rejection of the switching-frequency current ripple. On the other hand, from the inspection of Fig.8(b), it can be observed that the current loop has almost an unity gain at the lower frequencies. In particular, the magnitude- and phase-response at the fundamental frequency is 1.003 and −16.8 deg respectively. This is however not valid according to our findings, which can be proved with the simulation results presented in Fig.9. It can be noted that, actually, the magnitude of I_L is significantly reduced with respect to that of the reference signal I_L^*, which

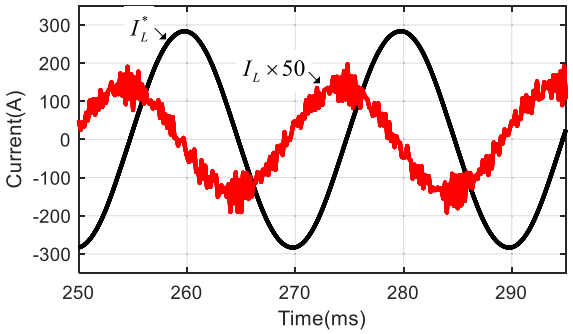

FIGURE 9. Simulation results of the inner-current loop with $K_C = K_C^{cmp}$ employed.

is certainly different from the previous theoretical findings draw from Fig.8(b).

The characteristic of the current loop is further investigated with the employment of the discrete model developed in this work. By substituting (6) into Fig.4(b), the transfer function representing the current loop can easily be obtained. Accordingly, the closed-loop frequency response is illustrated in Fig. 10, where $K_C = 2.3$ is firstly employed which will be proved in the following sections that it is the optimal choice for the case of Table 1. Some observations noted from the observation of Fig. 10 can be explained as follows.

- Magnitude response crosses through 0.707 at 524 Hz and 1506 Hz respectively. Thus, the closed-loop bandwidth can be deemed as 982 Hz, if the definition of bandwidth that the amplitude of the tracked signal is attenuated no more than 3 dB with respect to the original input signal is employed. It can also be observed that the magnitude response exhibits an amplification characteristic within the bandwidth, and reaches its peak value 4.0 at 1125 Hz, which is related to the filter resonance frequency ω_{res}.
- Alternatively, the magnitude response has very limited gain at lower frequencies. For instance, the magnitude is only 0.021 at the fundamental frequency, as depicted in the dotted box at the top-right corner of Fig. 10. Also, it can be noted that the phase response is significantly different from that of a common system, which instead of a phase-lag, is now a phase-lead characteristic, and it reaches as high as 85 deg at the fundamental frequency.

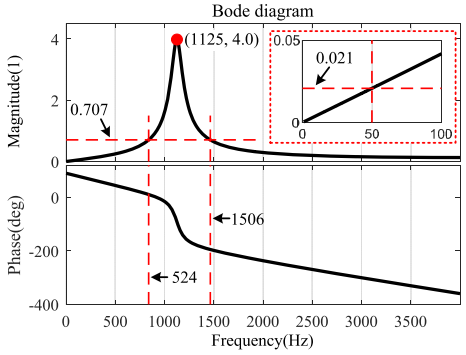

FIGURE 10. Closed-loop frequency response of inner-current loop.

In summary, the inner-current loop has a derivative characteristic with extremely attenuated magnitude around the fundamental frequency, which is in good agreement with the simulation findings presented in Fig. 9. As a result, it can be concluded that the current loop is not expected for accurate signal tracking in this case, which is totally different from the current regulation of grid-following converters. Therefore, performance evaluation based on the Bode diagram and loop bandwidth criterion, which is developed from grid-following converters, is no longer suitable for the current loop design of dual-loop controlled GFCs. It is therefore of permanent interest to develop an effective method to perform the analysis and design of the inner-current loop in this case.

B. ANALYSIS AND DESIGN OF THE INNER-CURRENT LOOP BASED ON THE DISCRETE ROOT LOCUS ANALYSIS

It is well known that the magnitude and damping ratio characteristics are commonly employed to evaluate the performance of a closed-loop pole. With the fact that the current loop is not developed for signal tracking identified previously, the magnitude characteristic which is related to the signal convergence speed, can therefore be ignored. Alternatively, the damping ratio which is directly related to stability, can be employed to investigate the active damping characteristic of the inner-current loop. Therefore, based on the discrete model of the plant established previously, a method for the current-loop design is developed in this section, which is achieved through damping optimazation with the help of the discrete root loci analysis. For subsequent analysis, it is necessary to establish the connection of the damping ratio of a close-loop pole in the z-domain with its correspondence in the s-domain, beginning with (12) for representing a general pole p_{cl}^s in the s-domain

$$p_{cl}^s = a \pm j \cdot b = \omega_0 \cdot \left(-\xi \pm j \cdot \sqrt{1-\xi^2}\right) \tag{12}$$

where a, b, ω_0, ξ are the real part, imagery part, magnitude and damping ratio of p_{cl}^s, respectively. It should be mentioned that $a < 0$, $b > 0$ is assumed here, which means p_{cl}^s is at the left half part of the s-plane, and hence stable.

Noting that $z = e^{s \cdot T_s}$, which upon combined with (12), gives rise to

$$p_{cl}^z = e^{-\xi \cdot \omega_0 \cdot T_s} \cdot \left[\cos\left(\omega_0 \cdot T_s \cdot \sqrt{1-\xi^2}\right) \pm j \cdot \sin\left(\omega_0 \cdot T_s \cdot \sqrt{1-\xi^2}\right)\right]. \tag{13}$$

Therefore, expression for relating the magnitude characteristic of a closed-loop pole in the z-domain and its correspondence in the s-domain can be derived from (13), which is given as follows:

$$\left|p_{cl}^z\right| = e^{-\xi \cdot \omega_0 \cdot T_s}. \tag{14}$$

Further noting that $a = -\xi \cdot \omega_0$, which combines with (14), yields

$$a = -\xi \cdot \omega_0 = \frac{\ln\left|p_{cl}^z\right|}{T_s}. \tag{15}$$

On the other hand, expression related to phase characteristic of (13) can be derived as follows:

$$\omega_0 \cdot T_s \cdot \sqrt{1-\xi^2} = \arctan\left(\frac{\mathrm{Im}\left(p_{cl}^z\right)}{\mathrm{Re}\left(p_{cl}^z\right)}\right). \tag{16}$$

Finally, the expression related to ξ can be derived from (15) and (16), which is expressed as follows:

$$\xi = \sqrt{\frac{1}{\left\{\arctan\left(\frac{\mathrm{Im}(p_{cl}^z)}{\mathrm{Re}(p_{cl}^z)}\right) \cdot \frac{1}{\ln\left|p_{cl}^z\right|}\right\}^2 + 1}}. \tag{17}$$

Therefore, with regard to a specified closed-loop pole p_{cl}^z, its damping ratio can be determined with (17) conveniently. To begin with, some observations noted from the inspection of Figs.2 and 3 for representing single- and dual-loop control schemes, can be explained as follows:

- As shown in Fig.2, for the single-loop control scheme, the original plant $V(z)/V^{\mathrm{PWM}}(z)$ along with z^{-1}, i.e. $V(z)/V_0(z)$, can be viewed as the equivalent plant of the voltage controller $C_{\mathrm{V}}(z)$.
- Similarly, for dual-loop control scheme, the original plant $V(z)/V^{\mathrm{PWM}}(z)$ together with z^{-1} and $C_{\mathrm{I}}(z)$, which is noted as $V(z)/I^*(z)$ in Fig.3, can be considered as the equivalent plant of the voltage controller $C_{\mathrm{V}}(z)$.

As proved earlier, for the single-loop voltage control, the equivalent plant $\frac{V(z)}{V^{\mathrm{PWM}}(z)} \cdot z^{-1}$ has two critical-stable conjugate poles resulted from filter resonance, which hence, makes the system hard to stabilize, as shown in Figs.5(a) and 6(a). Conceptually, if these poles cab be actively damped in the equivalent plant $V(z)/I^*(z)$ with the current gain K_{C}, an improved performance compared to that of single-loop control can be expected.

Under this consideration, the damping characteristic of $V(z)/I^*(z)$ is investigated, beginning with (18) for representing the equivalent plant of the voltage controller of dual-loop controlled GFCs

$$G_{\mathrm{PL}}^{\mathrm{Equ}}(z) = \frac{C_{\mathrm{I}}(z) \cdot [1-\cos(\omega_{res}T_s)] \cdot (z+1)}{z^3 - 2z^2\cos(\omega_{res}T_s) + (1+a)z - a} \tag{18}$$

where $a = C_{\mathrm{I}}(z) \cdot \sin(\omega_{res}T_s)/(\omega_{res}L)$.

The corresponding root locus of (18) is depicted in Fig.11(a), which is plotted by varying the current gain K_{C} at different resonance frequency ω_{res}. Some observations noted can be explained as follows:

- Trajectories started from $p_{ol}^{2,3}$ are different from that of Figs.5(b) and 6(b), which instead of always lie outside of the unit circle, is now moving inside of the unit circle at the beginning. Therefore, the pair of critical-damped poles $p_{ol}^{2,3}$ resulted from the filter resonance in (5), are actively damped and become stable in the equivalent plant of (18).
- However, with K_{C} continuous increasing, the trajectories will move toward to the unit circle, which means the damping ratio of the equivalent plant is decreasing. An interesting phenomenon can be noted that trajectories starting from p_{ol}^2 (or p_{ol}^3) of different ω_{res} will cross the boundary of the unit circle at the same point, which in Fig.11(b), is noted as point A. Also, if K_{C} increases continuesly, the trajectories will eventually move outside of the unit circle, which means the equivalent plant has become a non-minimum phase system with regard to the voltage controller $C_{\mathrm{V}}(z)$. This certainly should be avoided, as it will make the voltage loop hard to stabilize in this case.
- It worth noting that if p_{ol}^2 is located at the left part of the common crossing point A, then the plant cannot be damped by the employment of current loop any longer, as shown in Fig.11(b) for the case of ω_{res}^4. One way to overcome it is to reduce the resonance frequency and/or increase sampling frequency from (10).

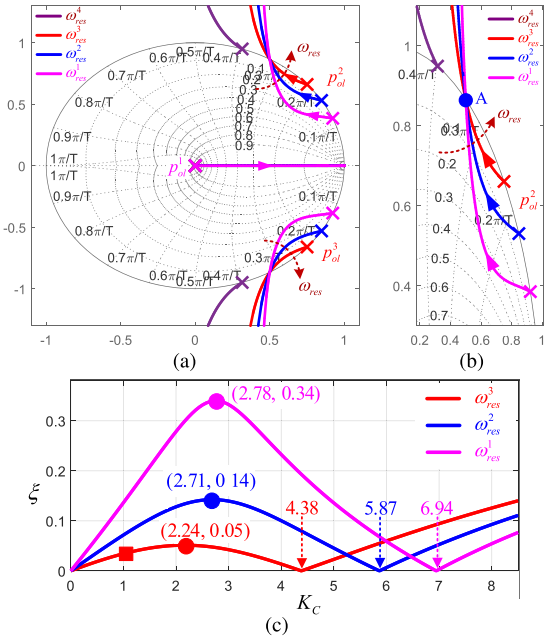

FIGURE 11. (a) root locus of (18) with the variation of K_{C} for different resonant frequency ω_{res}; (b) the detailed part of (a) around p_{ol}^2; (c) the relationship between damping ratio with respect to K_{C}.

To illustrate, the poles on the cures initiated from p_{ol}^2 can next be substituted into (17). The obtained damping ratio ξ with respect to K_{C} is depicted in Fig.11(c), where a parabolic shape representing the poles of Fig.11(b) within the unit circle can be noted. After that, damp ratio ξ increase sharply, which in practice, is related to the poles outside of the unit circle of Fig.11(b), and hence not considered. Regarding the parabolic shape, it can be noted that for a given ω_{res}, the damping ratio ξ reaches its peak value at a certain K_{C}, at which the plant is mostly damped. This value of K_{C} can thus be deemed as

the optimal gain K_C^{opt}, which theoretically, results the most enhanced stability for dual-loop controlled GFCs.

V. VOLTAGE LOOP DESIGN FOR DUAL-LOOP CONTROLLED GFCs

Following the method proposed above, the optimal gain K_C^{opt}=2.24 can be determined for the case of Table 1, which actually, is also the case of ω_{res}^3 in Fig.11, resulting in a determined equivalent plant in (18). Design of the voltage controller $C_V(z)$ in Fig.3 can then be continued. In particular, PR controller is employed for voltage regulation, whose parameter tuning is explained as follows, beginning with K_p to determine the overall stability margin.

As shown in Fig.12(a), Nyquist diagram of $K_p \cdot G_{PL}^{Equ}(z)$ for positive frequencies with different K_p is illustrated. The minimum value of the distance between the diagram at different frequencies and the critical point $(-1, j0)$, which is noted as $\eta = \min\left|1 + K_p \cdot G_{PL}^{Equ}(z)\right|$, is employed as a compact indictor of relative stability [35].

It can be noted that the Nyquist diagram exhibits an oval shape and η decreases sharply as K_p increases. It is worth noting that $\eta = 0.5$ for the case of $K_p = 0.028$. A good tradeoff between stability and avoidance of closed-loop anomalous peaks is thus achieved.

The next step is to decide the delay compensation φ for the resonance term in (7), which is also critical to the system's stability. In other words, the stability margin defined by K_p previously could be deteriorated if an inappropriate value of φ is employed. As shown in Fig.12(b), a asymptote at ω_e appears with resonance term $R_{rp}^{1d}(z)$ included. It can be noted that, for the case of $\varphi = 0$, η is reduced to 0.38, instead of 0.5 defined by K_p, which is certainly undesired. The solution is to adjust the angle between the asymptote and the real axis, which in Fig.12(b), is noted as $\theta = \pi/2 + \varphi + \angle G_{PL}^{Equ}(z)$. Typically, when the asymptote becomes vertical to the real axis, the system with most enhanced stability results, which have comprehensively been studied in [35]. The resulting Nyquist diagram with $\varphi = -\angle G_{PL}^{Equ}(z)$ has also been illustrated in Fig.12(b), where $\eta = 0.5$ is still retained.

High frequency resonance terms with ω_e replaced by $h\omega_e$ can then be included, whose delay compensation is $\varphi = -\angle G_{PL}^{Equ}(z)$ with $z = e^{j\cdot h\cdot\omega_e\cdot T_s}$ accordingly. In this manner, the asymptotes at each resonance frequency $h\omega_e$ will cross the real axis vertically, as shown in Fig.13(a) where h up to 19 are included. Regarding the close-loop frequency response, as shown in Fig.13(b), unity gains with no anomalous peaks at each of the desired frequencies have been achieved. Additionally, it should be emphasized that unless very large value of K_i is employed, it usually only influences the open-loop gains around its own resonance frequency. Therefore, K_i of different resonant terms can be tuned individually. In this work, K_i of the fundamental resonant term is tuned relatively larger than that of the higher frequency resonant terms, resulting in a higher bandwidth around the fundamental frequency than that of other harmonic

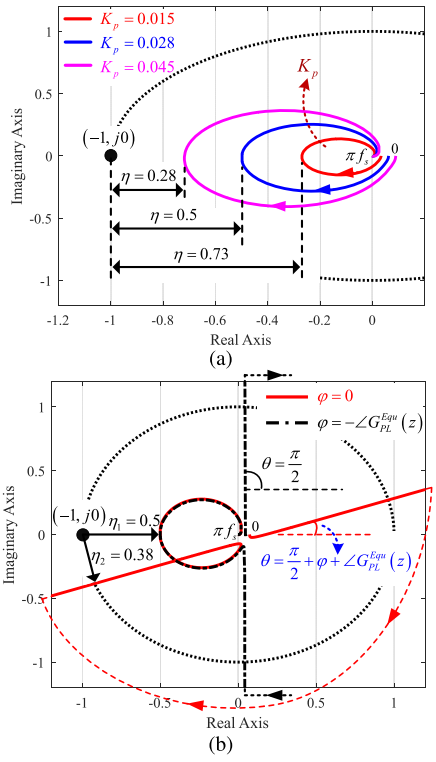

FIGURE 12. Nyquist diagram of (a) $K_p \cdot G_{PL}^{Equ}(z)$ and (b) $G_{PR}^{d}(z) \cdot G_{PL}^{Equ}(z)$ for positive frequencies.

frequencies, as depicted in Fig.13(b). In this manner, a fast transient response of the output voltage can be expected.

VI. EXPERIMENTAL RESULTS

The experimental setup is shown in Fig.14(a), where it can be noted that it consists of an input- and output-transformer, a diode rectifier, and an inverter. The input transformer, whose input- and output-voltage is 10kV and 500V at 50Hz respectively, as shown in Fig.14(b). Also shown in this figure is the output transformer, which is Δ/Y connected and the rated input- and output-voltage are both 380V at 50Hz, as shown in Figs.14(a) and (b). It should be noted that the primary voltage of the output transformer (i.e. the capacitor voltage), instead of the output voltage of the transformer, is sensed and fed back for regulation in this work. This is because the location of the output transformer is far from that of the converter, which is, therefore, inconvenient for signal sensing of the transformer output voltage. In this case, theoretically, the voltage droop cross the impedance of the transformer and the transmission line cannot be compensated by the controller. Therefore, for cases in which the load is very sensitive to this voltage droop, the output voltage of the transformer or the load voltage can be measured for regulation. Finally, the diode rectifier, the inverter, and the digital controller are depicted in Fig.14(c). The digital controller is mainly made of a DSP (TMS320F28335), an FPGA (EP2C5), and other auxiliary circuits for signal conditioning, analog to digital conversion and communication. Measuring

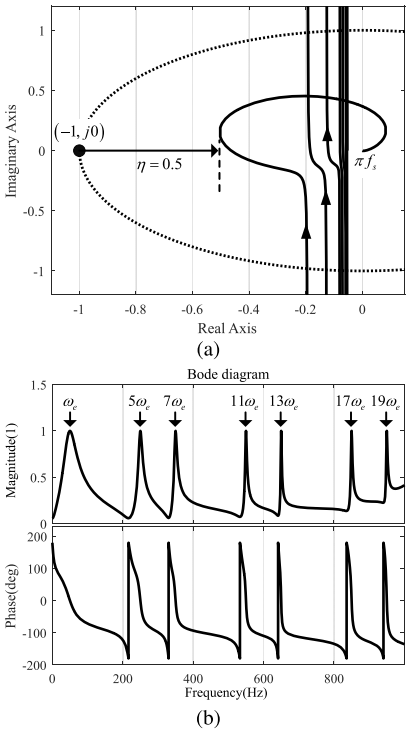

FIGURE 13. (a) Nyquist diagram and (b) closed-loop frequency response of voltage loop with resonant controller up to 19 are included.

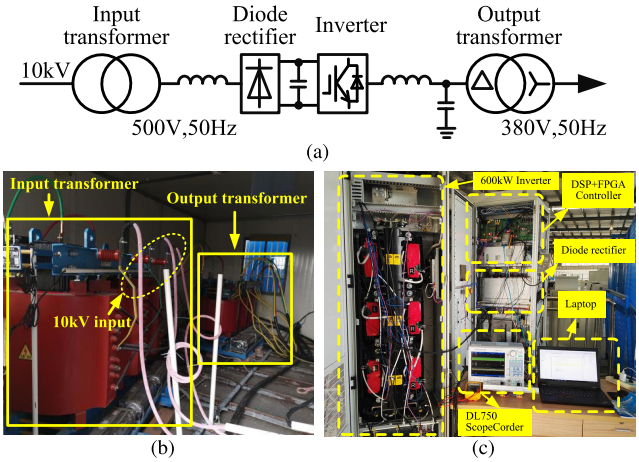

FIGURE 14. (a) block diagram and (b) (c) photograph of the experimental setup.

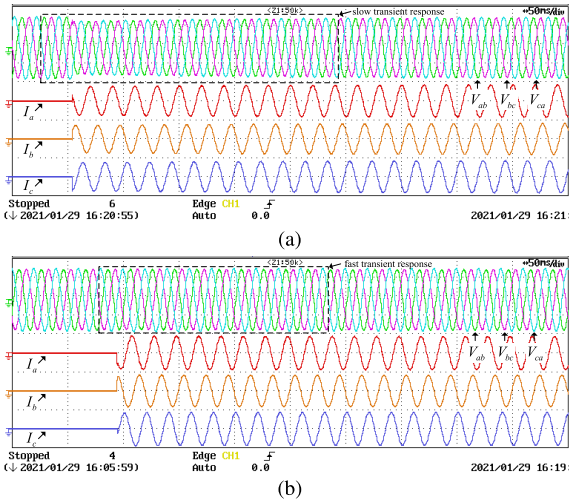

FIGURE 15. Experimental results for (a) single-loop and (b) dual-loop regulated GFCs.

equipment include a DL750 ScopeCorder, a PW3198 power quality analyzer, three differential probes and three current probes. Parameters of the setup are the same as those shown in Table 1. The signal sampling is performed at both peaks and valleys of the triangular carrier signal, which means the sampling frequency is twice of the switching frequency, as shown in Table 1. In particular, the ScopeCorder is set as follows: 1) CH1: dc-link voltage with 250V/div; 2) CH2 to CH4: V_{ab}, V_{bc}, and V_{ca} with 375V/div; 3) CH5 to CH7: i_a, i_b, and i_c with 100A/div.

Firstly, the performance of single-loop and dual-loop regulated GFCs are investigated. For the dual-loop method, K_C^{opt} is employed to achieve the optimum damping. As shown in Fig.15a, with the single-loop method employed, the output voltage exhibits a slow transient response when the converter is loaded, and the settling time is about 300ms. The reason for this lies in the constraint bandwidth as addressed in section III. This issue is however avoided by the employed of dual-loop method, as depicted in Fig.15b, where the magnitude of the output voltage is stable when the converter is loaded.

Then, the developed tuning method for the inner-current loop is investigated. The method derived from the loop-bandwidth criterion that is widely employed in the existing studies, i.e. $K_{\mathrm{C}}^{\mathrm{cmp}} = 1.072$, is employed for comparison, which in Fig.11, is noted as "■" for the case of ω_{res}^3. It can be observed that the damping ratio ξ of $K_{\mathrm{C}}^{\mathrm{cmp}}$ is significantly reduced compared to that of $K_{\mathrm{C}}^{\mathrm{opt}}$ which is noted as "●" for ω_{res}^3 in Fig.11.

Experimental results for the converter with three-phase balanced load is shown in Fig.16. It can be noted that there is a noticeable voltage sag with the load added for the case $K_{\mathrm{C}}^{\mathrm{cmp}}$, which is, theoretically, related to the low damping characteristic of the converter. In contrast, with $K_{\mathrm{C}}^{\mathrm{opt}}$ employed, the output voltage has almost no fluctuation when the converter is loaded, resulting in an improved performance compared to that of $K_{\mathrm{C}}^{\mathrm{cmp}}$. The root mean square (RMS) value of the output voltage for K_C^{cmp} and K_C^{opt} are both 387.5V.

In case of load imbalance, the experimental results are illustrated in Fig.17, where phase a is unloaded. Similarly, the transient performance of the output voltage for $K_{\mathrm{C}}^{\mathrm{opt}}$ is much improved with respect to that of $K_{\mathrm{C}}^{\mathrm{cmp}}$, which is resulted from the enhanced damping provided by $K_{\mathrm{C}}^{\mathrm{opt}}$. The RMS value of the output voltage for both cases are 387.6V, which can be noted form the left corner of Figs.17(a) and (b), respectively.

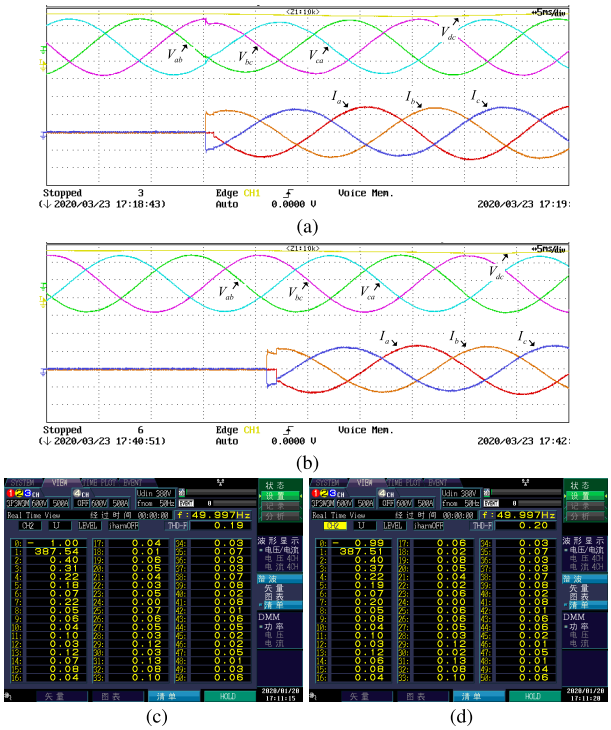

FIGURE 16. Experimental results for the converter with balanced load of (a) K_C^{cmp} and (b) K_C^{opt}.

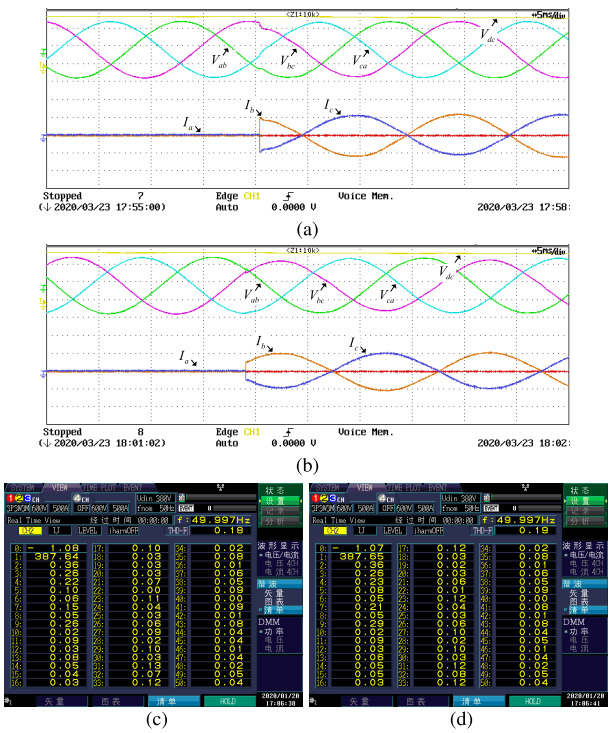

FIGURE 17. Experimental results for the converter with unbalanced load of (a) K_C^{cmp} and (b) K_C^{opt}.

The converter with nonlinear load is also investigated, which in this work, is a three-phase diode rectifier. If K_C^{cmp} is employed, the maximum h for resonant term is 7 for

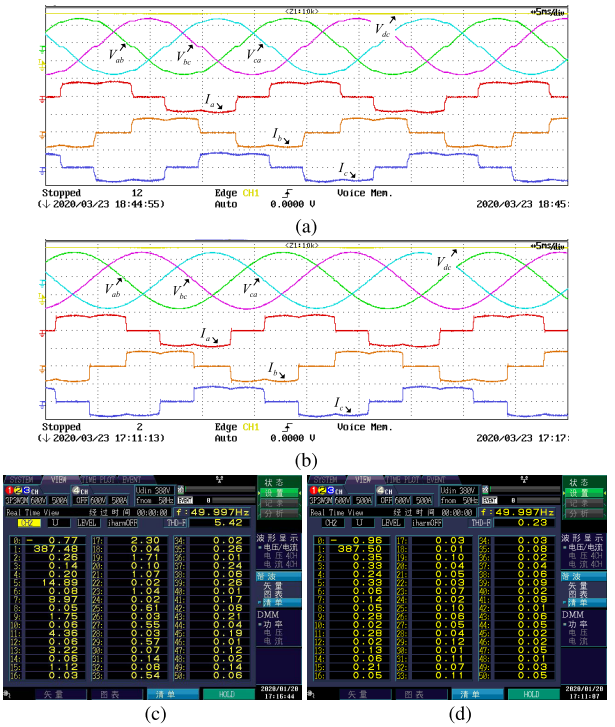

FIGURE 18. Experimental results for the converter with non-linear load of (a) K_C^{cmp} and (b) K_C^{opt}.

$C_V(z)$ to retain the stability margin defined by K_p, due to the limited damping of the equivalent plant in (18). In this case, the output voltage is high distorted, whose total harmonic distortion (THD) is 5.4%, as shown in Fig.18a. Alternatively, resonant terms of h up to 19 can be included for $C_V(z)$ if K_C^{opt} is employed, as shown in Fig.13. In this manner, the quality of the output voltage is much improved, as shown in Fig.18b, where the THD is reduced to 0.23%. It should be emphasized that the high-frequency signals up to 950 Hz are under control in this case, and the pulse ratio is extremely low with respect to the switching frequency which is 3 kHz, as shown in Table1.

VII. CONCLUSION

In this work, the single- and dual-loop control schemes for GFCs are deeply compared. The limitations of insufficient stability margin, constrained bandwidth and high sensitivity to parameter variation faced by single-loop voltage control are identified, if the resonant controllers are employed for voltage regulation. The essence of the inner-current loop is identified based on the discrete root locus analysis, and the criterion for current loop design has been addressed. To obtain the highest damping and most enhanced stability, a method for optimal tuning of the inner-current loop is developed, where the original plant with the one-sampling delay and the current gain are considered as the equivalent plant for the voltage controller, resulting in improved performance and disturbance rejection to the load.

REFERENCES

[1] Y. Han, H. Li, P. Shen, E. A. A. Coelho, and J. M. Guerrero, "Review of active and reactive power sharing strategies in hierarchical controlled microgrids," *IEEE Trans. Power Electron.*, vol. 32, no. 3, pp. 2427–2451, Mar. 2017.

[2] J. Liu, Y. Miura, and T. Ise, "Comparison of dynamic characteristics between virtual synchronous generator and droop control in inverter-based distributed generators," *IEEE Trans. Power Electron.*, vol. 31, no. 5, pp. 3600–3611, May 2016.

[3] M. Pradhan and M. K. Mishra, "Dual *P*–*Q* theory based energy-optimized dynamic voltage restorer for power quality improvement in a distribution system," *IEEE Trans. Ind. Electron.*, vol. 66, no. 4, pp. 2946–2955, Apr. 2019.

[4] J. Roldín-Pérez, A. Garcia-Cerrada, M. Ochoa-Gimenez, and J. L. Zamora-Macho, "Delayed-signal-cancellation-based sag detector for a dynamic voltage restorer in distorted grids," *IEEE Trans. Sustain. Energy*, vol. 10, no. 4, pp. 2015–2027, Oct. 2019.

[5] Z. Li, Y. Li, P. Wang, H. Zhu, C. Liu, and F. Gao, "Single-loop digital control of high-power 400-hz ground power unit for airplanes," *IEEE Trans. Ind. Electron.*, vol. 57, no. 2, pp. 532–543, Feb. 2010.

[6] M. Abarzadeh and K. Al-Haddad, "An improved active-neutral-point-clamped converter with new modulation method for ground power unit application," *IEEE Trans. Ind. Electron.*, vol. 66, no. 1, pp. 203–214, Jan. 2019.

[7] P. Mattavelli, "Synchronous-frame harmonic control for high-performance AC power supplies," *IEEE Trans. Ind. Appl.*, vol. 37, no. 3, pp. 864–872, 2001.

[8] P. C. Loh, M. J. Newman, D. N. Zmood, and D. G. Holmes, "A comparative analysis of multiloop voltage regulation strategies for single and three-phase UPS systems," *IEEE Trans. Power Electron.*, vol. 18, no. 5, pp. 1176–1185, Sep. 2003.

[9] M. Shahparasti, M. Mohamadian, A. Yazdian, A. A. Ahmad, and M. Amini, "Derivation of a stationary-frame single-loop controller for three-phase standalone inverter supplying nonlinear loads," *IEEE Trans. Power Electron.*, vol. 29, no. 9, pp. 5063–5071, Sep. 2014.

[10] S. Jiang, D. Cao, Y. Li, J. Liu, and F. Z. Peng, "Low-THD, fast-transient, and cost-effective synchronous-frame repetitive controller for three-phase UPS inverters," *IEEE Trans. Power Electron.*, vol. 27, no. 6, pp. 2994–3005, Jun. 2012.

[11] J. Chen, L.-J. Diao, L. Wang, H. Du, and Z. Liu, "Distributed auxiliary inverter of urban rail train—The voltage and current control strategy under complicated load condition," *IEEE Trans. Power Electron.*, vol. 31, no. 2, pp. 1745–1756, Feb. 2016.

[12] J. Chen, L. Wang, L. Diao, H. Du, and Z. Liu, "Distributed auxiliary inverter of urban rail train—Load sharing control strategy under complicated operation condition," *IEEE Trans. Power Electron.*, vol. 31, no. 3, pp. 2518–2529, Mar. 2016.

[13] X. Meng, J. Liu, and Z. Liu, "A generalized droop control for grid-supporting inverter based on comparison between traditional droop control and virtual synchronous generator control," *IEEE Trans. Power Electron.*, vol. 34, no. 6, pp. 5416–5438, Jun. 2019.

[14] X. Wang, P. C. Loh, and F. Blaabjerg, "Stability analysis and controller synthesis for digital single-loop voltage-controlled inverters," in *Proc. IEEE Appl. Power Electron. Conf. Expo. (APEC)*, Mar. 2016, pp. 2011–2018.

[15] P. C. Loh and D. G. Holmes, "Analysis of multiloop control strategies for LC/CL/LCL-filtered voltage-source and current-source inverters," *IEEE Trans. Ind. Appl.*, vol. 41, no. 2, pp. 644–654, Mar. 2005.

[16] X. Zhao, L. Meng, C. Xie, J. M. Guerrero, and X. Wu, "A unified voltage harmonic control strategy for coordinated compensation with VCM and CCM converters," *IEEE Trans. Power Electron.*, vol. 33, no. 8, pp. 7132–7147, Aug. 2018.

[17] F. M. M. Arani and Y. A.-R. I. Mohamed, "Dynamic droop control for wind turbines participating in primary frequency regulation in microgrids," *IEEE Trans. Smart Grid*, vol. 9, no. 6, pp. 5742–5751, Nov. 2017.

[18] M. Zhang, B. Song, and J. Wang, "Circulating current control strategy based on equivalent feeder for parallel inverters in islanded microgrid," *IEEE Trans. Power Syst.*, vol. 34, no. 1, pp. 595–605, Jan. 2019.

[19] R. M. Imran, S. Wang, and F. M. F. Flaih, "DQ-voltage droop control and robust secondary restoration with eligibility to operate during communication failure in autonomous microgrid," *IEEE Access*, vol. 7, pp. 6353–6361, 2019.

[20] M. V. Gururaj and N. P. Padhy, "A cost-effective single architecture to operate DC microgrid interfaced DFIG wind system during grid-connected, fault, and isolated conditions," *IEEE Trans. Ind. Informat.*, vol. 16, no. 2, pp. 922–934, Feb. 2020.

[21] J. Chen, J. Li, R. Qiu, and Z. Liu, "Control strategy of three-phase inverter with isolation transformer," *Energies*, vol. 12, no. 20, p. 4005, Oct. 2019.

[22] L. Diao, L. Wang, H. Du, L. Wang, Z. Liu, and S. M. Sharkh, "AI-HM based zero portion effects and phase-shift optimization for railway auxiliary inverter with pulsating DC-Link," *IEEE Access*, vol. 5, pp. 7444–7453, 2017.

[23] E. Alizadeh, A. M. Birjandi, and M. Hamzeh, "Decentralised power sharing control strategy in LV microgrids under unbalanced load conditions," *IET Gener., Transmiss. Distribution*, vol. 11, no. 7, pp. 1613–1623, May 2017.

[24] H. Li, Y. Han, P. Yang, J. Xiong, C. Wang, and J. M. Guerrero, "A proportional harmonic power sharing scheme for hierarchical controlled microgrids considering unequal feeder impedances and nonlinear loads," in *Proc. IEEE Energy Convers. Congr. Expo. (ECCE)*, Oct. 2017, pp. 3722–3727.

[25] P. P. Das, S. Chattopadhayay, and M. Palmal, "A d–q voltage droop control method with dynamically phase-shifted phase-locked loop for inverter paralleling without any communication between individual inverters," *IEEE Trans. Ind. Electron.*, vol. 64, no. 6, pp. 4591–4600, Jun. 2017.

[26] W. Wu, Y. Liu, Y. He, H. S.-H. Chung, M. Liserre, and F. Blaabjerg, "Damping methods for resonances caused by LCL-Filter-Based current-controlled grid-tied power inverters: An overview," *IEEE Trans. Ind. Electron.*, vol. 64, no. 9, pp. 7402–7413, Sep. 2017.

[27] R. Errouissi and A. Al-Durra, "Design of PI controller together with active damping for grid-tied LCL-filter systems using disturbance-observer-based control approach," *IEEE Trans. Ind. Appl.*, vol. 54, no. 4, pp. 3820–3831, Jul. 2018.

[28] D. Pérez-Estévez, J. Doval-Gandoy, A. G. Yepes, O. Lopez, and F. Baneira, "Generalized multifrequency current controller for grid-connected converters with LCL filter," *IEEE Trans. Ind. Appl.*, vol. 54, no. 5, pp. 4537–4553, Sep. 2018.

[29] Z. Xin, X. Wang, P. C. Loh, and F. Blaabjerg, "Grid-current-feedback control for LCL-filtered grid converters with enhanced stability," *IEEE Trans. Power Electron.*, vol. 32, no. 4, pp. 3216–3228, Apr. 2017.

[30] W. Wu, J. Liu, Y. Li, and F. Blaabjerg, "Individual channel design-based precise analysis and design for three-phase grid-tied inverter with LCL-filter under unbalanced grid impedance," *IEEE Trans. Power Electron.*, vol. 35, no. 5, pp. 5381–5396, May 2020.

[31] M. Monfared, S. Golestan, and J. M. Guerrero, "Analysis, design, and experimental verification of a synchronous reference frame voltage control for single-phase inverters," *IEEE Trans. Ind. Electron.*, vol. 61, no. 1, pp. 258–269, Jan. 2014.

[32] J. He and Y. W. Li, "Generalized closed-loop control schemes with embedded virtual impedances for voltage source converters with LC or LCL filters," *IEEE Trans. Power Electron.*, vol. 27, no. 4, pp. 1850–1861, Apr. 2012.

[33] J. He, B. Liang, Y. W. Li, and C. Wang, "Simultaneous microgrid voltage and current harmonics compensation using coordinated control of dual-interfacing converters," *IEEE Trans. Power Electron.*, vol. 32, no. 4, pp. 2647–2660, Apr. 2017.

[34] H. Komurcugil, N. Altin, S. Ozdemir, and I. Sefa, "An extended Lyapunov-function-based control strategy for single-phase UPS inverters," *IEEE Trans. Power Electron.*, vol. 30, no. 7, pp. 3976–3983, Jul. 2015.

[35] A. G. Yepes, F. D. Freijedo, Ó. Lopez, and J. Doval-Gandoy, "Analysis and design of resonant current controllers for voltage-source converters by means of Nyquist diagrams and sensitivity function," *IEEE Trans. Ind. Electron.*, vol. 58, no. 11, pp. 5231–5250, Nov. 2011.

[36] T. Nussbaumer, M. L. Heldwein, G. Gong, S. D. Round, and J. W. Kolar, "Comparison of prediction techniques to compensate time delays caused by digital control of a three-phase buck-type PWM rectifier system," *IEEE Trans. Ind. Electron.*, vol. 52, no. 2, pp. 791–799, Feb. 2008.

[37] V. Miskovic, V. Blasko, T. M. Jahns, A. H. C. Smith, and C. Romenesko, "Observer-based active damping of LCL resonance in grid-connected voltage source converters," *IEEE Trans. Ind. Appl.*, vol. 50, no. 6, pp. 3977–3985, Apr. 2014.

[38] Y. Wang, X. Wang, W. Xie, F. Wang, M. Dou, R. M. Kennel, R. D. Lorenz, and D. Gerling, "Deadbeat model-predictive torque control with discrete space-vector modulation for PMSM drives," *IEEE Trans. Ind. Electron.*, vol. 64, no. 5, pp. 3537–3547, May 2017.

[39] X. Zhang, P. Chen, C. Yu, F. Li, H. T. Do, and R. Cao, "Study of a current control strategy based on multisampling for high-power grid-connected inverters with an LCL filter," *IEEE Trans. Power Electron.*, vol. 32, no. 7, pp. 5023–5034, Jul. 2017.
[40] M. Lu, X. Wang, P. C. Loh, F. Blaabjerg, and T. Dragicevic, "Graphical evaluation of time-delay compensation techniques for digitally controlled converters," *IEEE Trans. Power Electron.*, vol. 33, no. 3, pp. 2601–2614, Mar. 2018. s
[41] X. Li, X. Wu, Y. Geng, X. Yuan, C. Xia, and X. Zhang, "Wide damping region for LCL-type grid-connected inverter with an improved capacitor-current-feedback method," *IEEE Trans. Power Electron.*, vol. 30, no. 9, pp. 5247–5259, Sep. 2015.

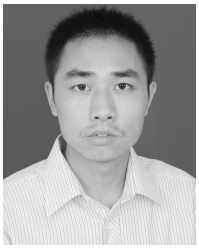

ZHIHONG ZHAO received the B.S. degree in electric engineering and automation from the China University of Petroleum, Qingdao, China, in 2008, and the M.S. and Ph.D. degrees in electric power engineering from Southeast University, Nanjing, China, in 2011 and 2017, respectively.

In 2017, he joined the Department of Electrical Engineering, School of Automation, Nanjing University of Science and Technology. His research interests include current control of grid-connected converters, active damping of LCL filter resonance, stability enhancement for parallel-connected converters, current control of converters in a weak grid, and virtual synchronous generator control.

ZHIPENG HAN received the B.S. degree in building electricity and intelligence from the Fujian University of Technology, Fuzhou, China, in 2017. He is currently pursuing the M.Eng. degree in electrical engineering with the Nanjing University of Science and Technology, Nanjing, China. His research interests include voltage control of inverters with LC filters, and parallel control of inverters.

XUNDUAN LIU received the B.E. degree in smart grid information engineering from the Nanjing University of Science and Technology, Nanjing, China, in 2018, where he is currently pursuing the M.E. degree in smart grid and control. His research interests include control and modulation strategy of VIENNA rectifier.

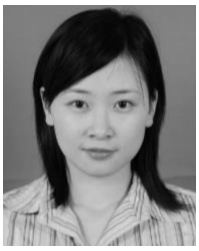

JIA YAO (Member, IEEE) was born in Nanjing, China. She received the B.Sc. and M.S. degrees in measuring and control technology, and the Ph.D. degree in electrical engineering from Southeast University, Nanjing, in 2002, 2005, and 2015, respectively. From 2005 to 2010, she was a Hardware/Senior Hardware Engineer with Mindray Medical Electronics International Corp. Ltd., Shenzhen, China. From 2012 to 2014, she was a Visiting Scholar with the University of California, Irvine, CA, USA. She is currently an Assistant Professor with the Electrical Engineering Department, Nanjing University of Science and Technology, Nanjing. Her current research interests include power electronics in power systems, high conversion ratio dc/dc converters, converter modeling, and photovoltaic/battery applications.

BAOJIAN JI received the B.S. degree in automation engineering from Nanjing Normal University, Nanjing, China, in 2002, the M.S. degree in electrical engineering from the Nanjing University of Aeronautics and Astronautics, Nanjing, in 2007, and the Ph.D. degree from Southeast University, Nanjing, in 2012.

In 2017, he was an Associate Professor with Nanjing Tech University, Nanjing, where he is currently the Head with the Department of Electrical Engineering. In 2018, he became an Associate Professor with the Nanjing University of Science and Technology, Nanjing. His research interests include digital control technique and development of grid-tied inverters for renewable energy.

SHUZHENG WANG received the Ph.D. degree in electrical engineering from Southeast University, Nanjing, in 2015. He is currently an Associate Professor with the Nanjing Institute of Technology and technical backbone at Jiangsu Province Intelligent Distribution Network Technology and the Equipment Collaborative Innovation Center. He is also mainly engaged in the teaching and research work of high-power multilevel converter technology, photovoltaic grid-connected technology, power quality assessment and management, flexible dc transmission, and distribution technology.

JIANFENG ZHAO received the B.S. degree in electrical engineering from Huainan Mining Institute, China, in 1995, the M.S. degree in automation from the Nanjing University of Aeronautics and Astronautics, Nanjing, China, in 1998, and the Ph.D. degree in electrical engineering from Southeast University, Nanjing, in 2001.

In 2001, he joined as a Faculty Member with the School of Electrical Engineering, Southeast University, where he has been a Professor, since 2008. He has been teaching and researching in the field of high-power electronics. He has been serving as the Dean of the School of Electrical Engineering, Southeast University, since 2014. He has authored more than 100 technical articles. He currently holds 50 Chinese patents and two U.S. patents. His main research interests include utility applications of power electronics in smart grids, such as solid-state transformers, active filters for power conditioning, flexible ac transmission system devices, multilevel ac motor drivers, and efficient energy utilization.